Modality of the tropical rain belt across models and simulated climates

Ori Adam,[a] Alexander Farnsworth,[b,c] Daniel J. Lunt,[b]

[a] *The Fredy and Nadine Herrmann Institute of Earth Sciences, The Hebrew University, Jerusalem, Israel*

[b] *School of Geographical Sciences and Cabot Institute, University of Bristol, Bristol, UK*

[c] *State Key Laboratory of Tibetan Plateau Earth System, Environment and Resources (TPESER), Institute of Tibetan Plateau Research, Chinese Academy of Sciences, Beijing, China*

Corresponding author: Ori Adam, ori.adam@mail.huji.ac.il

ABSTRACT: The tropical rain belt varies between unimodal and bimodal meridional precipitation distributions, both regionally and on seasonal to geological timescales. Here we show that this variation is largely driven by equatorial precipitation inhibition, and quantify it using an equatorial modality index (EMI) that varies continuously between 1 and 2 for purely unimodal and bimodal distributions. We show that tropical modality is a fundamental characteristic of tropical climate, which we define as annual-mean EMI. We examine large-scale aspects of tropical modality across 73 climate models from phases 5 and 6 of the coupled model intercomparison project, 45 paleo simulations (~300 million years ago to present), and observations. We find increased tropical modality to be strongly related to increased width of the tropical rain belt, wider and weaker meridional overturning circulation, colder equatorial cold tongues, and more severe double intertropical convergence zone bias in modern climate models. Tropical sectors (or global zonal means) with low tropical modality are characterized by monsoonal seasonal variations (i.e., seasonal migrations of rain bands following the Sun). In sectors with high tropical modality we identify three important seasonal modes: (i) migration of the precipitation distribution toward the warmer hemisphere, (ii) variation in the latitudinal separation between hemispheric rain bands, and (iii) seesaw variation in the intensity of the hemispheric rain bands. In high tropical modality sectors, due to contrasting shifts of the migration and separation modes, counter to general wisdom, seasonal migrations of tropical rain bands cannot be generally assumed to follow the Sun.

SIGNIFICANCE STATEMENT: The tropical rain belt is a band of intense precipitation that encircles the tropics. Important tropical phenomena such as monsoons and seasonal shifts of marine rain bands are driven by seasonal migrations of the tropical rain belt, which therefore govern key socio-economical aspects of tropical populations. This work examines how changes in the north-south profile of tropical precipitation affect large-scale aspects of tropical climate, on seasonal to geological timescales. Specifically, we examine the tendency of the profile of the tropical rain belt to vary from having one to two peaks (i.e., from being unimodal to bimodal). We define an objective quantitative measure of this modality variation, which varies between 1 and 2 for unimodal and bimodal profiles. We then show that the annual mean of this measure is an important general characteristic of tropical climate, which we define as tropical modality. We also show that in tropical regions where tropical modality is low (close to 1), rain bands follow the Sun in their seasonal migrations, and conform to the canonical model of the tropical overturning circulation, known as the Hadley circulation, which goes along with monsoonal seasonal variations. However, in regions with high tropical modality (i.e., close to 2), the common theoretical expectation that rain bands follow the Sun (or migrate toward the warming hemisphere) is not generally justified. Instead, we identify three important independent seasonal modes of variation: (i) migration of the precipitation distribution toward the warmer hemisphere, (ii) variation in the latitudinal separation between hemispheric rain bands (or width of the precipitation profile), and (iii) seesaw variation in the intensity of the hemispheric rain bands.

1. Introduction

The ascending branches of the tropical atmospheric overturning circulation, invigorated by convective latent heating, form heavy rains that encircle Earth, known as the tropical rain belt (Webster 2020). Seasonal migrations of the tropical rain belt drive key regional variations such as monsoons and shifts of marine rain bands, which affect vast tropical populations. Wide-ranging variations in the tropical rain belt throughout Earth's history challenge our understanding and provide insight on the nature of the climate system (Diaz and Bradley 2004; Schneider et al. 2014). However, limited paleo records and systematic biases in the representation of the tropical rain belt in modern climate models restrict our ability to explain past climates and to provide reliable predictions in a warming climate (Lin 2007; Bony et al. 2015; Harrison et al. 2015). Here we study a fundamental feature of the tropical rain belt: its variation between unimodal and bimodal meridional precipitation distributions, on seasonal to geological timescales. We show that this feature is important for understanding variations of the tropical rain belt across climates and for reconciling discrepancies across climate models.

In the present climate, the prevailing dynamical regime of the tropics is the Hadley circulation. The latitude of peak tropical precipitation (or maximal near-surface convergence) is accordingly generally identified as the intertropical convergence zone (ITCZ), where the southern and northern Hadley cells meet (Schneider et al. 2014; Berry and Reeder 2014). According to the Hadley circulation paradigm, a single ITCZ is expected to follow the Sun in its seasonal migrations. However, land-ocean contrast, cloud radiative effects, and atmosphere-ocean coupling, introduce asymmetries that cause the underlying characteristics of the tropical rain belt to significantly deviate from the idealized Hadley paradigm (e.g., Roberts et al. 2017; Kang 2020; Atwood et al. 2020; Adam 2021; Donohoe et al. 2021). Indeed, several studies found double ITCZs to be a prominent feature of the present climate, that varies by region and season (Zhang 2001; Gu et al. 2005; Adam et al. 2016b; Popp and Lutsko 2017; Donohoe et al. 2019). Zonally averaged, the observed tropical precipitation distribution is doubly peaked about the equator, and the relative strengths of the precipitation peaks vary considerably during the seasonal cycle (Webster 2020). Systematic biases in modern climate models, which persist since the earliest generations of comprehensive climate models, exaggerate this tendency for a doubly-peaked tropical precipitation distribution –

a problem commonly known as the double-ITCZ bias (Mechoso et al. 1995; Lin 2007; Adam et al. 2018a; Tian and Dong 2020).

It is therefore important to understand and correctly model the degree to which single or double ITCZs dominate the precipitation distribution. To this end, an objective quantitative measure of the modality of the tropical rain belt is required. More generally, for strongly bimodal distributions, common diagnostics of the tropical rain belt such as ITCZ position, width, and intensity, which stem from the Hadley circulation paradigm (Popp and Lutsko 2017; Byrne et al. 2018), may fail to optimally characterize variations of the tropical rain belt. Indeed, Donohoe et al. (2021) showed that unlike the common expectation from Hadley-like circulations, over a wide range of simulated climates with dominant double ITCZs, the variance explained by changes in the width and intensity of the tropical rain belt far exceeds that associated with ITCZ shifts. The importance of acknowledging tropical modality also extends to seasonal variations. Specifically, Zhao and Fedorov (2020) found that in the western Pacific, where rain bands reside on either side of the equator year round, seasonal variations are characterized by seesaw-like changes in the intensity of the hemispheric rain bands, rather than the Hadley-like seasonal migrations seen in other sectors. Adam (2021) further found that for bimodal precipitation distributions, the mean ITCZ position and the positions of hemispheric rain bands can shift in opposite directions. Improved understanding of the modes of variability associated with bimodal precipitation distributions may also help trace the origin of the double-ITCZ bias, which is linked to the sensitivity of the tropical rain belt to seasonal forcing (Bellucci et al. 2010; Li and Xie 2014; Adam et al. 2018a; Tian and Dong 2020; Kim et al. 2021).

Examples of modal variations in the tropical rain belt are shown in Fig. 1. In the present climate (Fig. 1a) the ITCZ is generally identified as the dominant tropical rain band in each region. In the Pacific, the rain band north of the equator is associated with the ITCZ, whereas the western rain band south of the equator is referred to as the south Pacific convergence zone (SPCZ; Vincent 1994). In the zonal mean, the existence of rain bands that straddle the equator, together with the tendency of the ITCZ to swiftly traverse the equator during transition seasons (Lindzen and Hou 1988; Dima and Wallace 2003), yield a northward-skewed doubly-peaked distribution. Figure 1b shows the tropical rain belt under pre-industrial conditions simulated by the UK Met Office HadCM3L model (HadCM3L version 4.5, see section 2 for more details on the HadCM3L simulations; Lunt et al.

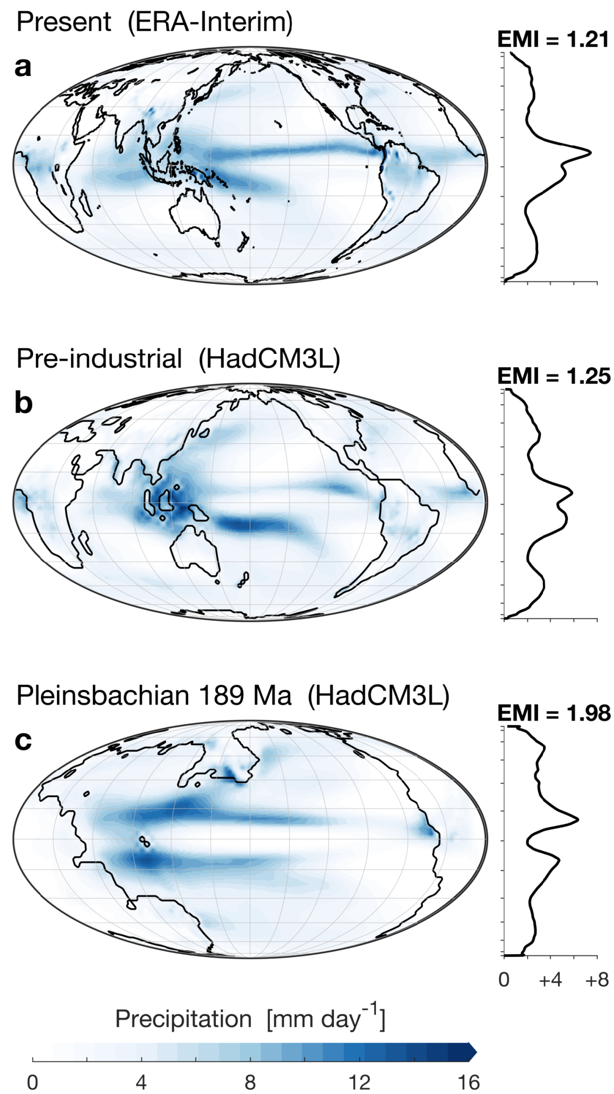

FIG. 1. Annual mean precipitation during (**a**) the present climate, and simulated (**b**) pre-industrial conditions, and (**c**) the Pleinsbachian period, 189 millions of years ago (Ma). Side panels show zonal means and tropical modality values (EMI, see section 3). Data taken from the European Center for Medium-Range Weather Forecasts (ECMWF) Interim Reanalysis (Dee et al. 2011) for the present climate (1979–2014), and simulations by the UK Met Office HadCM3L model, version 4.5 (Lunt et al. 2016).

2016). Excessive precipitation south of the equator in the Pacific (i.e., a double-ITCZ bias) causes the zonal-mean precipitation peaks that straddle the equator to be of equivalent strength, leading to a bimodal, mostly hemispherically symmetric precipitation distribution. The tropical rain belt under Pleinsbachian (189 millions of years ago) paleogeographic conditions, simulated by the

HadCM3L model, is shown in Fig. 1c. As in present day conditions, precipitation is stronger north of the equator. However, prominent rain bands that persist year-round on either side of the equator (supplemental Fig. S1), throughout a single wide ocean basin, lead to a skewed strongly bimodal distribution. Clearly, there are modal variations across the three examples. But how should these be quantified?

Here we address three main questions: (i) How can we objectively quantify the modality of the tropical rain belt? (ii) What are the large-scale variations associated with tropical modality? and (iii) How does the seasonal cycle of the tropical rain belt vary with modality? For robustness, we explore the relation of tropical modality to the tropical rain belt across a wide range of climate models, simulated climate states, and observations. Our analysis indicates that tropical modality binds together fundamental properties of the tropical rain belt and its associated overturning circulation. The data and methods are described in Section 2. Quantification of modality is discussed in Section 3. Large-scale, seasonal, and regional aspects of tropical modality are analyzed in sections 4 and 5, followed by summary and discussion in section 6.

2. Data and methods

a. Data

Observed reference data is taken from the European Center for Medium-Range Weather Forecasts (ECMWF) Interim Reanalysis (ERA-Interim; Dee et al. 2011) for the years 1979–2014. Net atmospheric energy input is calculated with mass-flux corrections that close the global energy budget, as described in Trenberth and Fasullo (2012). Our conclusions are not qualitatively sensitive to the choice of observed precipitation dataset, when compared with the National Oceanic and Atmospheric Administration's (NOAA) Global Precipitation Climatology Project version 2.2 (GPCP, Fig. S2a; Adler et al. 2003) and from the Climate Prediction Center Merged Analysis of Precipitation (CMAP, Fig. S2b; Xie and Arkin 1996).

We analyze variations across 42 climate models from phase 5 (Taylor et al. 2012) and 31 models from phase 6 (Eyring et al. 2016) of the coupled model intercomparison project (CMIP5/6), based on availability (supplemental Tables 1-2). For each model we use monthly data from the first realization (r1i1p1 for CMIP5 and r1i1p1f1 for CMIP6) of historical simulations (coupled climate models with present day atmospheric composition and radiative forcing). No critical distinctions were found in the representation of the tropical rain belt between the two CMIP phases (Tian and Dong 2020; Samuels et al. 2021), which are therefore analyzed jointly. For consistency, analyses of climate models and observations are performed on monthly climatologies derived from the years 1979–2005, linearly interpolated to a 1°×1° horizontal grid (the results, which involve calculations of large scale variations, are not sensitive to this interpolation).

We also analyze variations of monthly climatologies across multiple paleo climate simulations carried out using the UK Met Office HadCM3L climate model (v4.5), which includes cloud and vegetation feedbacks (Valdes et al. 2017). The model has 19 vertical levels in the atmosphere and 20 vertical levels in the ocean, with a horizontal resolution of 3.75°longitude by 2.5°latitude. Details on the model configuration and setup for these simulations can be found in Lunt et al. (2016). The model uses present day orbital parameters and fixed CO_2 concentration of 1120 ppmv. Climate variations are generated by changing the solar constant following Gough (1981, the solar constant monotonically increases with time by 2.5% over the past 300 Ma) and paleogeographic boundary conditions, taken from reconstructions of 44 geological stages, spanning 300–35 Ma (Lunt et al. 2016; Jones et al. 2019). Due to the fixed CO_2 concentration, global mean temperature variations in the simulated stages are significantly smaller than in paleo records. An additional simulation of pre-industrial conditions was analyzed, in which CO_2 concentration is set to 280 ppmv. Due to this disparity in CO_2 concentration, pre-industrial conditions are omitted in our analyses of variations across the simulated stages. The land masks, annual mean precipitation, and vertical wind at 500 hPa in each of these simulations are shown in the SM, sorted by age (Figs. S3-4).

As shown in Fig. 1b, the HadCM3L model has a strong double-ITCZ bias, suggesting that biased representation of the tropical rain belt exists in all of the simulated geological states. However, the variations in the tropical rain belt across simulated climates are far greater than the precipitation biases associated with the double-ITCZ bias (Fig. S3). Therefore, while acknowledging the limitations of the HadCM3L simulations (i.e., double-ITCZ bias and limited global mean temperature variations due to fixed CO_2 concentration), we interpret the suite of simulations across multiple geological stages as providing valuable information about climatic variations in the tropical rain belt and its associated large-scale tropical overturning circulation. Similarly, we interpret CMIP5/6 simulations as representing variations across climate models, which may include systematic model biases (e.g., the double-ITCZ bias). The joint analysis of variations across CMIP5/6 models and

HadCM3L simulated climates therefore reduces the sensitivity of our analysis to specific climate models or climate states, allowing us to identify robust aspects of tropical modality. For simplicity, the joint dataset is referred to as CMIP5/6 and HadCM3L simulations.

b. Calculation of large-scale parameters

We explore the relation of variations in tropical modality to key large-scale parameters, listed below:

- Global mean temperature (GMT) is calculated from near-surface (2m) air temperature;
- Tropics to poles temperature difference (TPTD) is calculated from near-surface air temperature as the difference between area-weighted mean temperature equatorward of 20° and poleward of 70° (the results are not qualitatively sensitive to variations of these meridional boundaries within ±10°);
- Atmospheric net energy input (NEI) is calculated as net radiative energy input at the top-of-atmosphere and at the surface, together with surface latent and sensible heat fluxes into the atmosphere. Equatorial NEI (NEI_0) is calculated as the average of NEI equatorward of 5° (Adam et al. 2016a);
- A cold tongue index (CTI) in CMIP5/6 models is calculated as the mean sea surface temperature (SST) equatorward of 6° between 180°E–270°E, minus global mean SST (Deser and Wallace 1990). In HadCM3L simulations, where the width of the main ocean basin varies between different paleogeographies, CTI is calculated as the mean SST equatorward of 6° in the 25–75% quartiles of the zonal distance between the warmest and coldest equatorial points in the widest ocean basin, minus global mean SST;
- The meridional overturning circulation (MOC) width is calculated as the distance between the poleward edges of the hemispheric Hadley cells, which are calculated as subtropical zero crossings of the meridional mass streamfunction at 500 hPa in each hemisphere, using the TropD software package (Adam et al. 2018b);
- MOC intensity is defined as the sum of the absolute extremal values of the meridional mass streamfunction in each hemisphere;

- ITCZ width, defined as the width of the rising branch of the MOC, is calculated as the latitudinal distance between the northern and southern tropical extrema of the mass streamfunction at 500 hPa (Byrne et al. 2018);

- Walker circulation (WC) intensity is calculated as the maximal difference between the 200 hPa and 850 hPa levels of the annual-mean zonally varying zonal wind, averaged equatorward of 10°. In HadCM3L simulations, due to varying ocean basin width, the maximal difference is calculated from all longitudes (i.e., the Walker circulation is defined as the predominant zonal overturning circulation); in CMIP5/6 models and in HadCM3L pre-industrial conditions, it is calculated in the Pacific [100°E–280°E].

We also characterize seasonal variations using parameters derived from the first four (area-weighted) moments of the zonal mean precipitation distribution: (i) the precipitation centroid (ϕ_{cent} or m_1), (ii) standard deviation σ ($\sqrt{m_2}$), (iii) skewness (m_3), and (iv) kurtosis (m_4) (Wilks 2011). Using curly brackets to denote the integral over tropical latitudes equatorward of ϕ_T=30°,

$$\{(\cdot)\} \equiv \int_{-\phi_T}^{\phi_T} (\cdot)\cos(\phi)\mathrm{d}\phi \tag{1}$$

the moments are calculated as

$$\phi_{cent} \equiv m_1 = \frac{\{P(\phi)\phi\}}{\{P(\phi)\}} \tag{2a}$$

$$m_2 = \frac{\{P(\phi)(\phi-\phi_{cent})^2\}}{\{P(\phi)\}} \tag{2b}$$

$$m_3 = \frac{1}{m_2^{3/2}}\frac{\{P(\phi)(\phi-\phi_{cent})^3\}}{\{P(\phi)\}} \tag{2c}$$

$$m_4 = \frac{1}{m_2^{2}}\frac{\{P(\phi)(\phi-\phi_{cent})^4\}}{\{P(\phi)\}} \tag{2d}$$

where P denotes zonal mean precipitation. The precipitation centroid is a common metric for the position of the ITCZ (Frierson and Hwang 2012; Donohoe et al. 2013; Adam et al. 2016a). The standard deviation provides a measure of the width of the tropical rain belt (Pearson coefficient of correlation R of annual mean σ with ITCZ width is 0.60 and 0.87 across CMIP5/6 and HadCM3L simulations). However, since bimodal distributions are considered, it should not generally be used to infer normal distribution characteristics. The skewness provides a measure of the asymmetry of the distribution with respect to the precipitation centroid. It vanishes for a Gaussian precipitation distribution that migrates meridionally, and increases as the precipitation distribution leans toward the northern hemisphere (i.e., the precipitation centroid is north of the maximal value). Skewness therefore indicates the degree of hemispheric asymmetry of the precipitation distribution. The kurtosis increases with the weight of the tails of the precipitation distribution; it therefore complements the indices introduced in the next section, which vary with normalized equatorial precipitation.

The latitudes of the precipitation peaks in each hemisphere are calculated using

$$\phi_{peak} = \frac{\int_{\phi_1}^{\phi_2} \phi \, (\cos(\phi) P)^n \, \mathrm{d}\phi}{\int_{\phi_1}^{\phi_2} (\cos(\phi) P)^n \, \mathrm{d}\phi} \tag{3}$$

where ϕ_1 and ϕ_2 denote meridional integration boundaries, and n acts as a smoothing parameter (reducing grid dependence), yielding the precipitation centroid for $n = 1$ (Eq. 2a) and the latitude of maximal precipitation for large n (Adam et al. 2018b). Northern and southern hemisphere tropical precipitation peaks (ϕ^{N} and ϕ^{S}) are calculated using $n = 10$ and $[\phi_1, \phi_2] = [0, 30°\mathrm{N}]$ and $[30°\mathrm{S}, 0]$, respectively, across all datasets.

3. Quantifying tropical modality

The zonal-mean precipitation and vertical wind for the examples in Fig. 1 are shown in Fig. 2, decomposed into hemispherically symmetric and anti-symmetric components (the corresponding meridional overturning circulations are shown in Fig. S5). We first note that, with some variation, the bimodal character of each of the examples persists during solstitial seasons (Fig. 2, left panels, thin lines). Specifically, the annual-mean bimodal precipitation distributions are characterized by off-equatorial peaks and an equatorial dip, which closely follow the vertical wind (cf. Fig. S6 showing an even better agreement of precipitation minus evaporation with the vertical wind). The equatorial dip, which is the key contributing factor to the bi-modality of the precipitation distributions, persists during solstitial seasons, and is linked only to the hemispherically symmetric

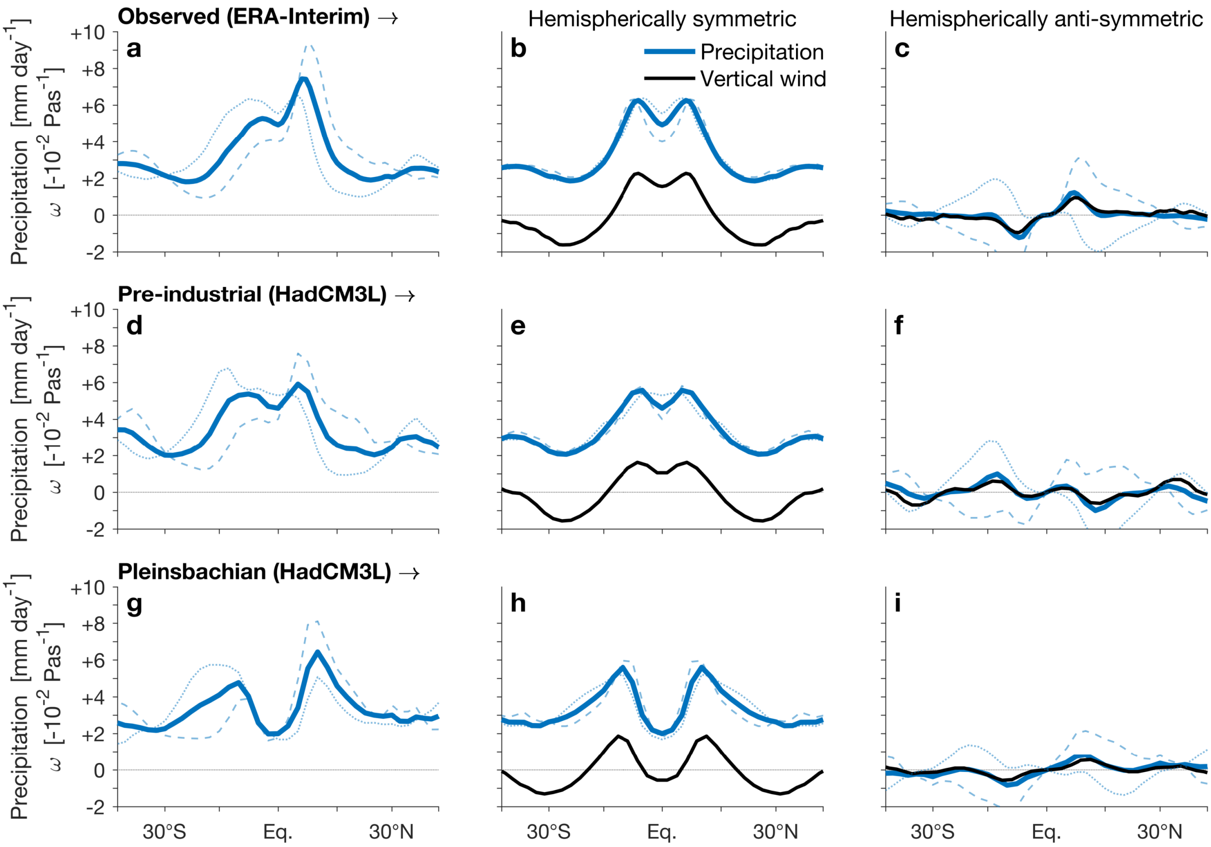

FIG. 2. Zonal-mean precipitation (blue) and vertical wind (ω, black, negative scaling) for observed conditions (upper panels), and for pre-industrial (mid row) and Pleinsbachian (189 Ma, lower panels) conditions simulated by the HadCM3L model, as in Fig. 1. For precipitation, annual means are shown in bold lines and Jun–Aug and Dec–Feb means are shown in thin dashed and dotted lines, respectively. Middle and right panels show the hemispherically symmetric and hemispherically anti-symmetric components, respectively, of precipitation and ω. The hemispherically symmetric and anti-symmetric components are calculated as $A^{\text{symmetric}} = \frac{1}{2}\left[A(\phi) + A(-\phi)\right]$ and $A^{\text{anti-symmetric}} = \frac{1}{2}\left[A(\phi) - A(-\phi)\right]$, respectively, where ϕ denotes latitude and A is some zonal-mean field.

component (mid panels; the anti-symmetric component vanishes identically at the equator, as seen in the right panels of Fig. 2). The above examples therefore indicate that: (i) the modality of the tropical rain belt is closely related to the mean overturning circulation (MOC), and (ii) that tropical modality is particularly closely related to equatorial precipitation inhibition, which is itself a feature only of the hemispherically symmetric precipitation distribution. We therefore base our quantification of tropical modality on equatorial precipitation inhibition.

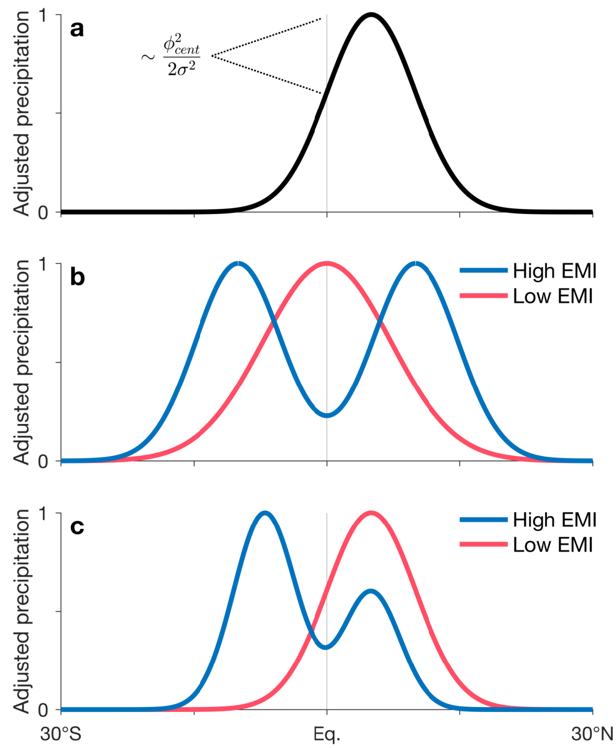

FIG. 3. (**a**) Depiction of the change in equatorial precipitation caused by off-equatorial shifts of a Gaussian precipitation distribution (shift correction in Eq. 4). (**a**,**b**) Depictions of tropical precipitation distributions yielding high- and low-EMI values for hemispherically symmetric and asymmetric conditions.

To quantify equatorial precipitation inhibition, we assume two contributions to equatorial precipitation: (i) a component related to the hemispherically symmetric circulation, as shown in Fig. 2; and (ii) changes in equatorial precipitation caused by meridional shifts of the precipitation distribution, which do not affect modality, as depicted in Fig. 3a. We accordingly define an Equatorial Modality Index (EMI) as

$$\mathrm{EMI} = 2 - \alpha \frac{P_0 + \frac{\phi^2_{cent}}{2\sigma^2}}{\overline{P}}. \tag{4}$$

Here the zonal mean tropical precipitation [30°S–30°N] is adjusted such that its minimal and maximal values are [0 1], and P_0 and $\overline{P}$ denote adjusted zonal mean precipitation at the equator and averaged over the latitudes 30°S–30°N, respectively (to reduce grid dependence, P_0 is calculated by linear interpolation at the equator). The term $\phi^2_{cent}/2\sigma^2$ is a first order approximation of the change in equatorial precipitation for a Gaussian function shifted off the equator and normalized between

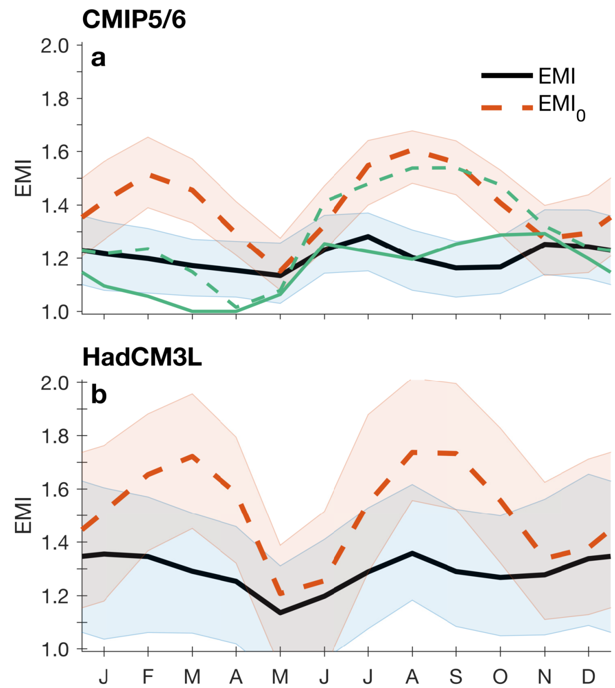

FIG. 4. Seasonal cycle of EMI (solid) and EMI without the shift correction (EMI_0, dashed) for (**a**) CMIP5/6 simulations and ERA-Interim (green); (**b**) HadCM3L simulations. Bold lines show ensemble means; shadings show ± 1 standard deviation across CMIP5/6 and HadCM3L simulations (blue for EMI and red for EMI_0).

[0 1] (Fig. 3a). EMI approaches 2 in the limit of vanishing adjusted equatorial precipitation, indicating a strictly bimodal distribution. The coefficient $\alpha = 0.45$ is empirically set based on the CMIP5/6 and HadCM3L simulations to make annual mean EMI approach 1 when the adjusted precipitation distribution is maximal at the equator. Values calculated using Eq. (4) bellow 1 are set to 1. This constrains EMI values to the range [1 2], such that for Eq. (4) values smaller or larger than [1 2], precipitation distributions are assumed to be invariantly strictly unimodal or bimodal. For clarity, the terms 'low' and 'high' tropical modality are used throughout this work to indicate EMI values nearing 1 and 2 (i.e., unimodal and bimodal distributions), as opposed to modality in general, which implies unbounded variation in the number of modes. Depictions of low- and high-EMI precipitation distributions are shown in Fig. 3b-c for hemispherically symmetric and asymmetric conditions.

To illustrate the effect of the Gaussian shift correction ($\phi_{cent}^2/2\sigma^2$), Fig. 4 shows EMI and EMI calculated without this correction (EMI_0), derived from monthly climatological means (note that EMI_0 is similar to the equatorial precipitation index derived in Adam et al. 2016c). In

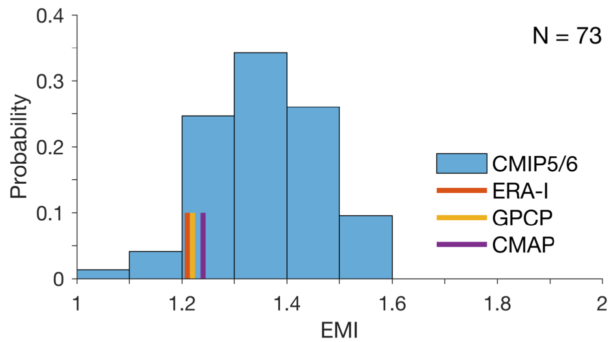

FIG. 5. (**a**) Probability distribution function of EMI derived from annual mean precipitation in the 73 CMIP5/6 historical simulations (Tables S1-2). Vertical bars show observed values from the ERA-Interim (ERA-I, orange), GPCP (yellow), and CMAP (purple) datasets.

contrast to the strong seasonal variations in EMI_0, caused by the seasonal migrations of the ITCZ, EMI shows nearly constant values year-round, while maintaining a rather uniform spread across models and simulated climates. Annual mean EMI values derived from monthly climatological means are slightly smaller than those derived from annual mean precipitation; nevertheless, the two are extremely well correlated (coefficient of correlation across the CMIP5/6 and HadCM3L simulations is 0.99). Therefore, we base our analysis hereon on EMI derived from long-term means. We interpret this value as a general climate characteristic, which we refer to as "tropical modality". Tables S1-2 and Figs. S3-4 show the EMI values for each CMIP5/6 and HadCM3L simulation.

Figure 5 shows the probability distribution function of EMI values for the 73 CMIP5/6 models. All of the EMI values are larger than 1 (Tables S1-2), so that the distribution function is unaffected by constraining EMI values to the range [1 2]. As expected from the double-ITCZ bias, modeled values are generally higher than observed (CMIP5/6 mean EMI is 1.36, compared to 1.21, 1.22, and 1.24, in the ERA-Interim, GPCP, and CMAP datasets, respectively).

High- and low-EMI composites of tropical precipitation distributions are shown in Fig. 6. As expected, in the HadCM3L simulations, which cover a wide range of climate states, low- and high-EMI composites are strongly unimodal and bimodal, respectively. In the CMIP5/6 historical simulations, low-EMI models show higher equatorial precipitation and smaller differences between equatorial precipitation and the peaks that straddle the equator (Popp and Lutsko 2017). Low-EMI

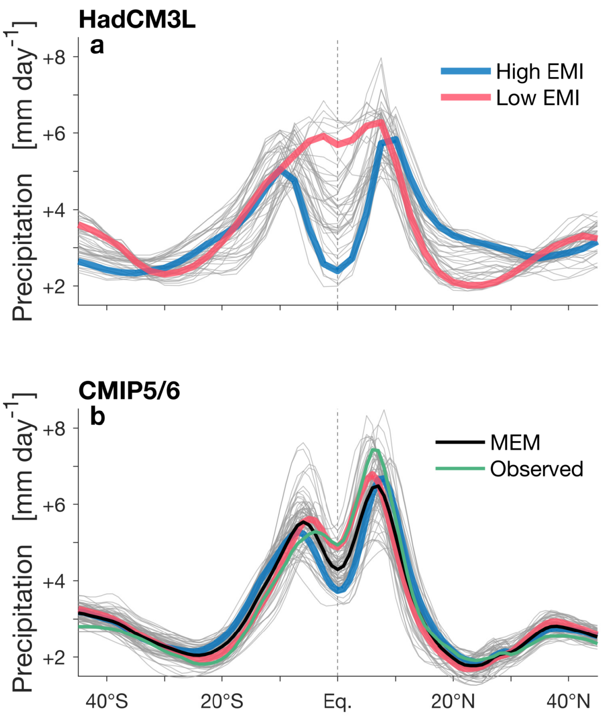

Fig. 6. Zonally averaged annual-mean precipitation in each of the (**a**) HadCM3L simulated climates (gray), and (**b**) CMIP5/6 historical simulations (gray). Composites of high- and low-EMI profiles are shown in blue and red, corresponding to lowest and highest 10 cases for HadCM3L simulations and 15 CMIP5/6 models. Panel **b** also shows the model ensemble mean (MEM, black) across CMIP5/6 models, and observed values taken from ERA-Interim (green).

models therefore show significantly reduced double-ITCZ bias, as well as reduced biases near the equator.

Figure 7a,b shows the variation of EMI and global mean temperature (GMT) across the HadCM3L simulations. GMT variations in paleo records are generally not captured by the HadCM3L simulations, in which CO_2 levels are fixed. Nevertheless, minimal tropical modality (EMI$\approx$ 1) is seen around the Cretaceous thermal maximum (~85–90 Ma, O'Brien et al. 2017), preceded by a monotonic transition from maximal tropical modality (EMI$\approx$ 2) during the early to mid Cretaceous (~145–100 Ma). A dramatic increase in tropical modality is seen during the Triassic, which in paleo records is characterized by global cooling, following the hothouse climate of the late Permian (Hannisdal and Peters 2011). It is also interesting to note that in the simulated stages, the tropics to poles temperature difference (TPTD, Fig. 7c) is generally maximal during the Cretaceous and

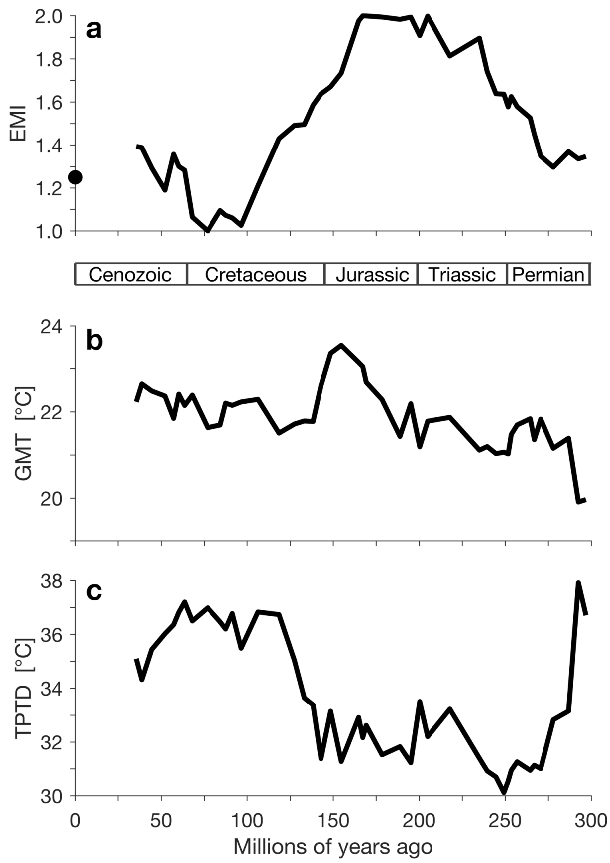

FIG. 7. Values in each of the HadCM3L simulated stages of the (**a**) equatorial modality index (EMI), (**b**) global mean temperature (GMT), and (**c**) tropics to poles temperature difference (TPTD). CO_2 concentrations during pre-industrial conditions are significantly lower than in other geological stages, resulting in significantly lower GMT and higher TPTD values (15.8 and 48.5 °C, respectively), which are therefore not shown.

minimal during the late Permian, in accordance with paleo records (Taylor et al. 1992; Rees et al. 2002; O'Brien et al. 2017). The variation of tropical modality with observed GMT records, as well as with decreasing TPTD despite nearly fixed simulated GMTs, suggests that tropical modality is strongly linked to the topical atmospheric and ocean overturning circulations, which govern poleward energy transport (Goddéris et al. 2014). We further explore the relation of tropical modality to large-scale aspects of the MOC in the next section.

4. Large-scale aspects of tropical modality

Since equatorial precipitation inhibition is closely linked to the MOC, EMI is indirectly related to phenomena in subtropical and even extratropical latitudes, which covary with the MOC. This is

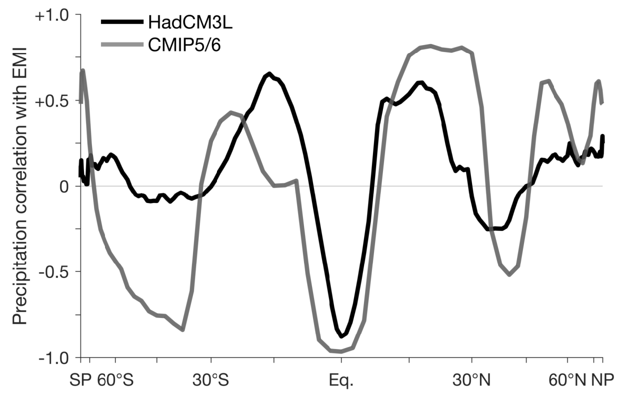

FIG. 8. Correlations of the equatorial modality index (EMI) with annual-mean zonally-averaged precipitation minus evaporation across the CMI5/6 models (black) and HadCM3L simulations (gray), per latitude.

evident in Fig. 8, showing correlations of EMI with zonal mean precipitation minus evaporation (which closely follows the mean vertical wind, as seen in Fig. S6) in the CMIP5/6 and HadCM3L simulations (cf. Fig. 1 in Adam et al. 2016c). Table 1 summarizes the correlations of EMI with large-scale parameters across the CMIP5/6 and HadCM3L simulations. EMI is positively correlated with the width of the MOC and with the width of the ITCZ, and negatively correlated with the intensity of the MOC across CMIP5/6 and HadCM3L simulations (cf. Fig. S5 where the MOC is wider and weaker under Pleinsbachian conditions). Due to the small variations in global mean temperature (GMT) across both CMIP5/6 and HadCM3L simulations, EMI is not significantly correlated with GMT (R = -0.08 and 0.09, respectively). Nevertheless, due the known strong correlation of GMT with ITCZ width and with MOC width and intensity (Byrne et al. 2018; Staten et al. 2018), GMT does not act as a confounding factor in the correlations shown in Table

TABLE 1. Correlations of EMI with: tropics to poles temperature difference (TPTD), equatorial atmospheric net energy input (NEI_0), cold tongue index (CTI), MOC width and intensity, Walker circulation (WC) intensity, and ITCZ width, across the CMIP5/6 and HadCM3L simulations. Correlations with 95% confidence levels are bolded.

$R(\mathrm{EMI}, \cdot)$	TPTD	NEI_0	CTI	MOC width	MOC intensity	WC intensity	ITCZ width
CMIP5/6	-0.16	**-0.52**	**-0.49**	**0.44**	**-0.50**	0.17	**0.70**
HadCM3L	**-0.68**	**-0.65**	**-0.91**	**0.88**	**-0.81**	**0.69**	**0.86**

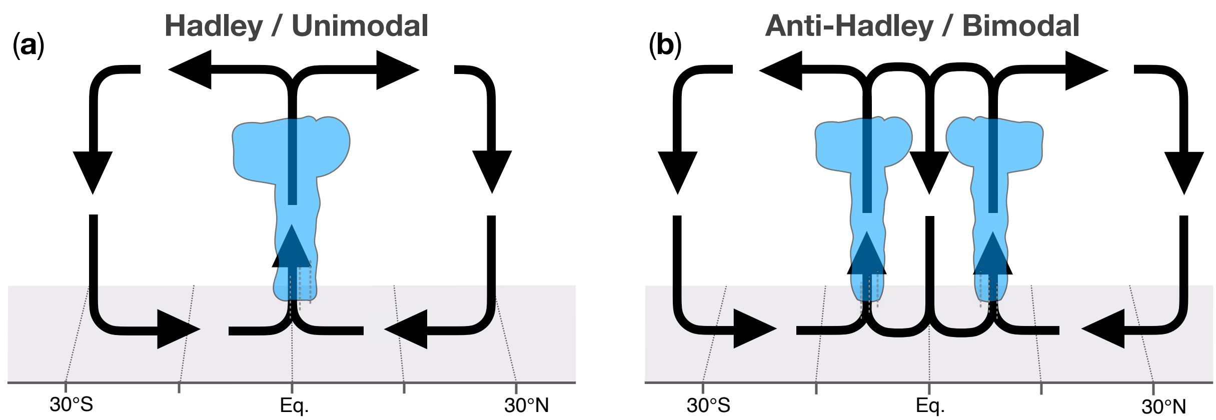

FIG. 9. Depictions of hemispherically symmetric (**a**) Hadley and (**b**) anti-Hadley circulations, and their relation to single (unimodal) and double (bimodal) ITCZs.

1, thus raising the confidence of the statistical relations between EMI and each of the large-scale parameters.

Cursory examination of the variations in paleogeography, precipitation, and circulation in the HadCM3L simulations (Figs. S3-4) suggests that tropical modality increases with the width of the dominant ocean basin. However, the effects of additional confounding variables affecting equatorial precipitation inhibition such as boundary layer, cloud, and ocean dynamics must also be considered. Specifically, in the present climate, the equatorial cold tongues that emerge in the Pacific and Atlantic due to wind-driven ocean circulation inhibit precipitation by stabilizing the atmospheric column and by suppressing surface convergence (Lindzen and Nigam 1987; Philander et al. 1996). Indeed, EMI is negatively correlated with the cold tongue index (CTI), indicating increased equatorial precipitation inhibition as the cold tongue intensifies. Consistent with this relation, EMI is also positively correlated with Walker circulation intensity, which is dynamically linked to the cold tongue strength via the Bjerknes feedback (Bjerknes 1969; Webster 2020). This correlation, however, is significant only in the HadCM3L simulations, pointing to the important role of paleogeography.

Convective dynamics can also inhibit equatorial precipitation, and can lead to doubly-peaked tropical precipitation distributions, even for a static ocean (Möbis and Stevens 2012; Blackburn et al. 2013; Voigt et al. 2014; Medeiros et al. 2015; Popp and Silvers 2017; Talib et al. 2018). Given the diversity of mechanisms that determine the distribution of the tropical rain belt, an energetic approach has been shown to simplify the analysis and effectively capture bifurcations from single

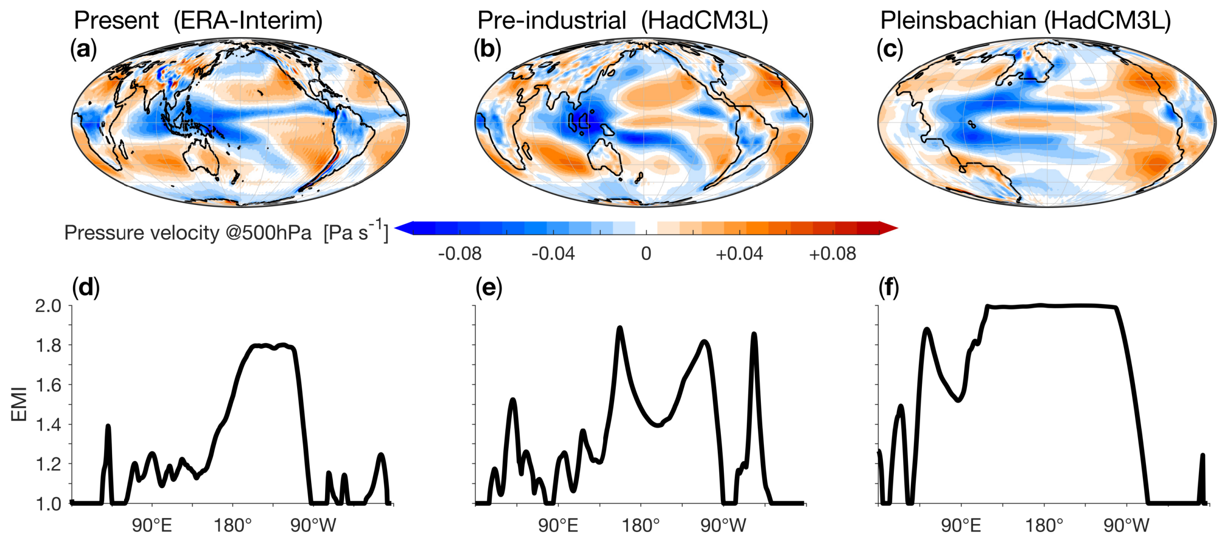

FIG. 10. Upper panels: Annual mean vertical pressure velocity at the 500 hPa level during (**a**) the present climate, and simulated (**b**) pre-industrial conditions, and (**c**) the Pleinsbachian period (189 Ma). Lower panels: the corresponding zonally varying EMI calculated using running sector means of 10°.

to double ITCZs (Bischoff and Schneider 2016; Adam et al. 2016b). Specifically, a deficit in energy input into the atmosphere at the equator (i.e., lower NEI_0), caused by either dynamic or convective processes (Talib et al. 2018), or by increased equatorial ocean heat uptake at the cold tongues (Adam 2021), can lead to a meridional overturning circulation that transports energy toward the equator (Bischoff and Schneider 2016). This circulation can be described as anti-Hadley, with ascending branches on either side of the equator and a descending branch at the equator (Fig. 9). EMI is indeed negatively correlated with NEI_0, in accordance with the expectation of bifurcation to double ITCZs as NEI_0 decreases (Bischoff and Schneider 2016; Adam et al. 2016b). Similarly, elevated EMI in CMIP5/6 models (Fig. 5) is consistent with the double-ITCZ bias in CMIP5/6 models, which goes along with a too cold and westward extended Pacific cold tongue (Mechoso et al. 1995; Li and Xie 2012; Zheng et al. 2012), and lower than observed NEI_0 (Adam et al. 2018a; Kim et al. 2021).

The relation of EMI and the MOC can be further understood by examining the zonal variation in the tropical vertical wind and in EMI, as shown in Fig. 10 (the same plot with hemispherically symmetric vertical wind is shown in Fig. S7). The regional MOC in sectors with a rising branch at the equator can be described as Hadley-like (characteristic of monsoonal regions; Dima and

Wallace 2003); sectors with an equatorial descending branch and ascending branches that straddle the equator can be characterized as having anti-Hadley-like regional MOC, which occurs mostly over oceans along cold tongues (Bischoff and Schneider 2016; Adam et al. 2016b; Adam 2021). (We note, however, that the sector mean vertical wind is also strongly affected by the zonal overturning circulation; Raiter et al. 2020; Galanti et al. 2022). As seen in Fig. 10, the zonal variation from Hadley-like to anti-Hadley-like sector-mean MOC follows EMI. Zonal mean EMI can therefore be interpreted as describing the relative contributions of regions with Hadley- and anti-Hadley-like circulations. Thus, for example, in the present climate Hadley-like circulation dominates in most sectors, leading to a low-EMI climate; in contrast, under Pleinsbachian conditions anti-Hadley-like circulation dominates in most sectors, leading to a high-EMI climate. We note, however, that in the present climate, the low EMI in the Asian monsoon sector may result from the persistent rain band in the southern Indian ocean (Zhang et al. 2022), rather than the Hadley-like monsoonal variations.

We next turn to examining the differences in the seasonal cycle between low- and high-EMI climates, which, as can be inferred from the above discussion, also vary regionally.

5. Seasonal and regional aspects of tropical modality

a. Seasonal variations of the zonal mean precipitation distribution

Monthly climatologies of statistical properties of the zonal-mean tropical precipitation distribution in the CMIP5/6 and HadCM3L simulations are shown in Fig. 11, with high- and low-EMI composites denoted by blue and red lines. Low-EMI climates and models show:

i. Reduced extent of seasonal migrations by the mean position of the ITCZ (as captured by the precipitation centroid, Fig. 11a,b);

ii. Reduced width of the tropical rain belt (as captured by the standard deviation of zonal mean tropical precipitation, Fig. 11c,d, consistent with Table 1);

iii. Reduced seasonal skewness (Fig. 11e,f); and

iv. Increased kurtosis (Fig. 11g,h).

These characteristics are consistently seen across the CMIP5/6 and HadCM3L simulations, but are generally not statistically significant for the CMIP5/6 historical simulations in which inter-model

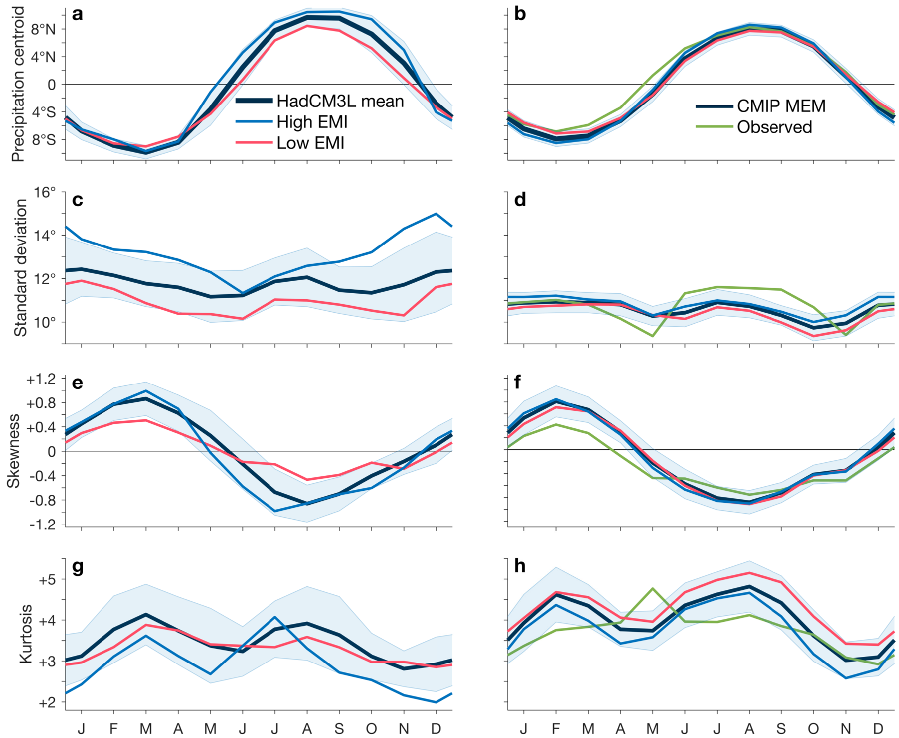

FIG. 11. Monthly climatologies of statistical properties of the zonal mean tropical precipitation distribution for HadCM3L simulations (left panels), CMIP5/6 historical simulations (right panels), and observations (ERA-Interim, green, right panels). Shown are the (**a**,**b**) precipitation centroid, (**c**,**d**) standard deviation, (**e**,**f**) skewness, and (**g**,**h**) kurtosis. CMIP5/6 and HadCM3L model ensemble means (MEM) are shown in black. High- and low-EMI composites are shown in blue and red, corresponding to lowest and highest 10 cases for HadCM3L simulations and 15 CMIP5/6 models. Blue shading indicates ±1 standard deviation across CMIP5/6 and HadCM3L simulations.

variance is weaker. We therefore conclude that tropical modality has the potential to efficiently differentiate seasonal variations of the tropical rain belt, as represented by the first four moments.

For CMIP5/6 models, consistent with the double-ITCZ bias, excessive seasonal migrations of the precipitation centroid during the southern hemisphere rainy season (Li and Xie 2014; Adam et al. 2018a) go along with coincident positive biases in both skewness and kurtosis. Since equatorial precipitation is strongly influenced by the seasonal migrations of the ITCZ across the equator (Fig. S8), the excessive migrations in CMIP5/6 models lead to a semi-annual variation in kurtosis, which is not seen in the present climate.

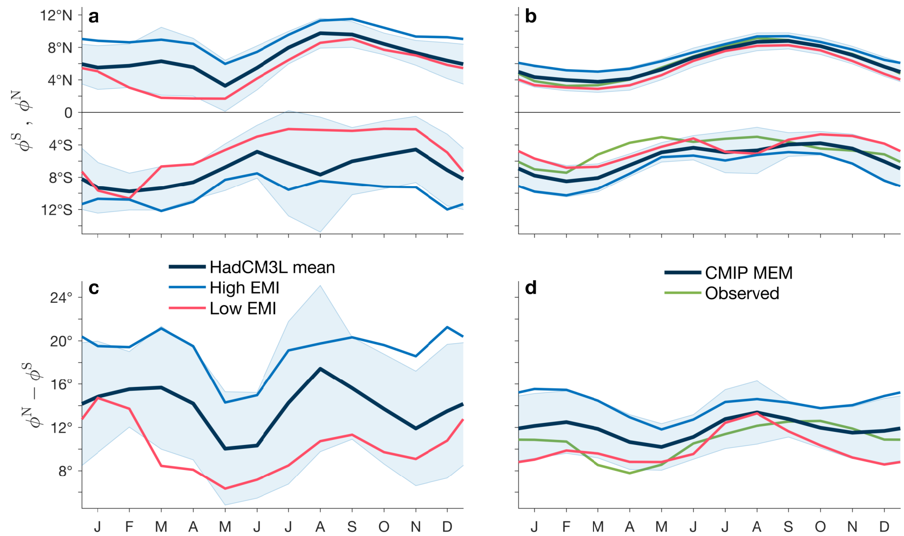

FIG. 12. Monthly climatologies of the positions of the northern and southern peaks in zonal-mean tropical precipitation (ϕ^N and ϕ^S, respectively; upper panels), and the latitudinal separation between ϕ^N and ϕ^S (lower panels), for HadCM3L simulations (left panels), CMIP5/6 historical simulations (right panels), and observations (ERA-Interim, green, right panels). CMIP5/6 and HadCM3L model ensemble means (MEM) are shown in black. High- and low-EMI composites are shown in blue and red, corresponding to lowest and highest 10 cases for HadCM3L simulations and 15 CMIP5/6 models. Blue shading indicates ±1 standard deviation across CMIP5/6 and HadCM3L simulations.

b. Seasonal variations of hemispheric rain bands

The seasonal properties of the tropical precipitation distribution can also be understood by considering seasonal variations of the hemispheric rain bands. As shown below, additional degrees of freedom become important with increasing tropical modality. Figure 12 shows the seasonal migrations of the precipitation peaks north (ϕ^N) and south (ϕ^S) of the equator. To ensure only doubly-peaked distributions are considered, the calculations in Fig. 12 are done only for CMIP5/6 and HadCM3L simulations with EMI greater than 1.1, so that the low-EMI composites have EMI values somewhat larger than the composites shown in other plots.

The hemispheric peaks generally migrate seasonally following the Sun (Fig. 12 upper panels), but also show a semi-annual variation in the latitudinal separation between the peaks (Fig. 12 lower panels), in accordance with the semi-annual cycle in kurtosis and equatorial precipitation (Figs. 11g-h and S8). Therefore, in addition to the mean position of the ITCZ, which is captured by the

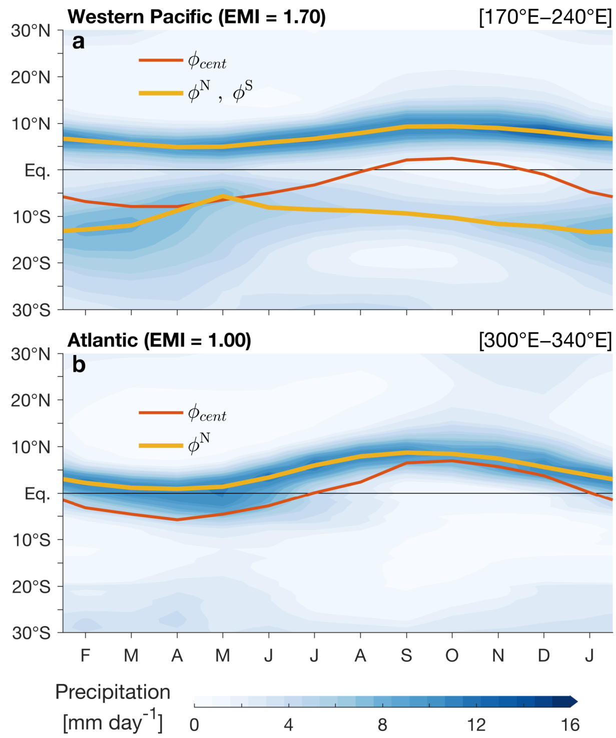

FIG. 13. Seasonal cycle of the observed meridional marine precipitation distributions in (**a**) the western Pacific sector [170°E–240°E], and (**b**) the Atlantic sector [300°E–340°E]. Orange and yellow lines show the locations of the sector-mean precipitation centroid (ϕ_{cent}) and of the northern and southern rain bands (ϕ^{N}, ϕ^{S}), respectively.

precipitation centroid (ϕ_{cent}), tropical modality introduces an additional degree of freedom, which can be interpreted as the separation between the northern and southern peaks ($\phi_{sep} = \phi^{N} - \phi^{S}$). This can also be interpreted as variation in the width of the tropical rain belt (correlation of ϕ_{sep} with ITCZ width is 0.92 and 0.82 for the CMIP5/6 and HadCM3L simulations, respectively).

Thus, in the limit of a strictly unimodal distribution, consistent with the Hadley paradigm, the precipitation centroid captures the seasonal migrations of the ITCZ. However, as tropical modality increases, the precipitation centroid captures only the general tendency of the precipitation distribution to shift toward the warmer hemisphere, and the separation between hemispheric peaks provides additional critical information. In the annual mean, the correlation between the ϕ_{sep} and ϕ_{cent} is generally weak (0.37 across HadCM3L simulations and 0.04 across CMIP5/6 models, with p-values 0.01 and 0.7, respectively), indicating that ϕ_{cent} and ϕ_{sep} (or ITCZ width) indeed provide generally independent information.

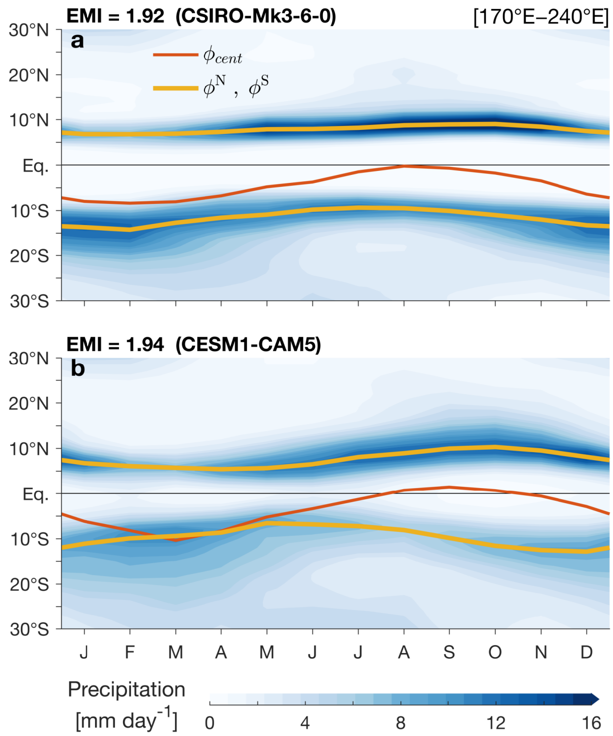

FIG. 14. As in Fig. 13, for the CSIRO-Mk-6-0 and CESM1-CAM5 CMIP5 models, both with high-EMI values in the western Pacific.

c. Seasonal and regional variations of hemispheric rain bands

The differences between unimodal and bimodal precipitation distributions are also seen across regions. Fig. 13 contrasts the observed seasonal cycles in the Pacific, characterized by a bimodal precipitation distribution (regional EMI = 1.70), and the Atlantic, characterised by a unimodal precipitation distribution (EMI = 1.00). In the Atlantic, a single ITCZ migrates seasonally but remains north of the equator year-round. In accordance with the Hadley paradigm, the precipitation centroid closely covaries with the position of the northern precipitation peak. Moreover, since in the Atlantic a single rain band migrates back and forth, the seasonal contrast in precipitation is significant (i.e., monsoonal-like). In contrast, in the western Pacific, the northern rain band migrates with the precipitation centroid, but at a much lower amplitude. As a result, seasonal precipitation contrasts are weak. Further, the southern rain band (deep tropical branch of the SPCZ) shifts counter to the precipitation centroid during boreal summer. Consistent with seasonal variations in the strength of the Pacific cold tongue, the northern and southern rain bands are nearest during boreal spring, when the cold tongue is weakest (van der Wiel et al. 2016; Adam 2018).

Finally, as shown by Zhao and Fedorov (2020) and Adam (2021), for high-EMI regions or climate states, changes in the intensity of the hemispheric rain bands become important. Fig. 14 shows the seasonal variation in the western Pacific for two climate models with high EMI values in the western Pacific. In the SCIRO-Mk3-6-0 model, hemispheric ITCZs remain mostly stationary year round, and the seasonal variation is characterized primarily by seesaw changes in precipitation intensity. In contrast, for the CESM1-CAM5 model, all three of the seasonal modes mentioned above are important: (i) migration of the precipitation distribution following the Sun (captured by the precipitation centroid), (ii) variation in the separation between the hemispheric rain bands (captured by ϕ_{sep} or ITCZ width), and (iii) seesaw changes in the intensity of the hemispheric rain bands.

6. Summary and discussion

The tropical rain belt is composed of rain bands that lie along the rising branches of the tropical overturning circulation. The modality of the zonal mean tropical precipitation distribution is therefore strongly linked to the overturning circulation regime of the tropics. In the present climate, the prevailing tropical circulation regime is the Hadley circulation, which under ideal conditions leads to a unimodal precipitation distribution. However, regional and meridional deviations from idealized Hadley circulation give rise to precipitation distributions that vary between uni- and bi-modality. Here we show that modality is an essential characteristic of the tropical rain belt, which "summarizes our ignorance" (borrowing a phrase from Neelin and Held 1987) of the underlying dynamic and convective processes that give rise to key properties of the tropical rain belt.

We quantify the modality of the tropical rain belt using an Equatorial Modality Index (EMI) that increases in proportion to equatorial precipitation inhibition, and varies continuously between 1 and 2 (uni- and bi-modality; Eq. 4). We define EMI calculated from the long-term mean of the tropical precipitation distribution as "tropical modality", which we argue is a general characteristic of tropical climate.

We examine variations of the tropical rain belt across observations, 73 historical simulations of models from phases 5 and 6 of the coupled model intercomparison project (CMIP5/6, Tables S1-2), and 45 simulations by the UK Met Office HadCM3L model with varying paleogeographic conditions spanning the past 300 million years (Figs. S3-4). Using these datasets, which represent variations across a diversity of climate models and simulated climate states, we identify robust large-scale aspects of tropical modality.

Since equatorial precipitation inhibition is closely linked to the mean overturning circulation (MOC), EMI is strongly correlated with large-scale processes in equatorial, subtropical, and even extratropical latitudes (Fig. 8 and Table 1). Specifically, it is associated with increased cold-tongue strength and reduced equatorial atmospheric net energy input, which both inhibit equatorial precipitation (Bischoff and Schneider 2016; Adam et al. 2016b). EMI is also negatively correlated with the intensity of the Hadley circulation, and positively correlated with the total width of the tropical MOC, as well as with the width of its rising branch (ITCZ width). In the HadCM3L simulations, despite generally negligible changes in global mean temperature (due to fixed CO_2 levels), the tropics to poles temperature difference (TPTD) decreases with EMI, pointing to the important role of the large-scale circulation regime in regulating poleward energy transport (Goddéris et al. 2014).

The seasonal cycle of the tropical rain belt is particularly sensitive to variations in tropical modality. Specifically, increased tropical modality is found to be associated with wider excursions of the mean position of the ITCZ, increased width of the tropical rain belt, increased seasonal skewness of the precipitation distribution, and reduced kurtosis (Fig. 11). These characteristics can vary across regions. For example, in the observed climate, the precipitation distribution is strongly bimodal in the western Pacific and unimodal in the Atlantic (Figs. 10, 13).

For unimodal precipitation distributions (either regional or in the zonal mean), the dominant seasonal mode is migration of rain bands following the Sun (monsoonal mode, Fig. 13b). In contrast, for bimodal distribution we identify three critical seasonal modes of variation:

i. Migration of the precipitation distribution toward the warmer hemisphere, which is captured by the precipitation centroid (migration mode);

ii. Variation in the separation between hemispheric rain bands (separation mode); and

iii. Seesaw variation in the intensity of hemispheric rain bands (seesaw mode).

Here we distinguish between the monsoonal mode, which characterizes unimodal distributions and leads to large seasonal contrasts, and the migration mode for bimodal distributions, which does not necessarily lead to strong seasonal contrasts. In addition, for bimodal distributions showing distinct hemispheric rain bands (e.g., Fig. 14a), while the latitudinal distance between the hemispheric peaks ϕ_{sep} is well correlated with indices of the width of the precipitation distribution (i.e., ITCZ width and σ), ϕ_{sep} is nevertheless a more appropriate descriptor.

The seasonal modes described above, which depend on tropical modality, project onto annual mean variations in the mean position, width, and intensity of the precipitation distribution (Donohoe et al. 2021), and are therefore critical for understanding variations of the tropical rain belt on seasonal to geological timescales. In the present climate, this is particularly true in the tropical western Pacific, which is strongly bimodal (Fig. 13a). Indeed, Zhao and Fedorov (2020) found that the seesaw mode dominates seasonal variations in the western Pacific. Similarly, Yan et al. (2015) found that the precipitation response in the western Pacific to the volcanic eruptions that instigated the Little Ice Age is inconsistent with the commonly assumed monsoonal mode. The notorious double-ITCZ bias in modern climate models can also be described as a positive bias in Pacific tropical modality.

More generally, for climate conditions with large tropical modality, failure to account for all three of the above mentioned modes may lead to erroneous interpretations. For example, Adam (2021) showed that wind-driven ocean energy transport generally damps shifts of the precipitation centroid but can amplify shifts of hemispheric precipitation peaks – stressing the need to consider both the migration and separation modes. Moreover, under some conditions, the separation mode can counter the migration mode, such that hemispheric rain bands cannot be assumed to always follow the Sun in their seasonal migrations (e.g., Figs. 13a and 14b, southern ITCZ during boreal autumn).

Finally, here we argue that the concept of tropical modality is important for understanding and describing variations in the tropical rain belt. We propose EMI as an objective quantitative measure of tropical modality. But other measures may be similarly effective, such as ITCZ width (Byrne et al. 2018), geometric characterizations of the precipitation distribution (Popp and Lutsko 2017; Donohoe et al. 2021), or measures based on the mean overturning circulation. Important aspects of tropical modality such as its relation to the zonal overturning circulation, global mean temperature, systematic precipitation biases in climate models, and climate variability, have only been briefly addressed here and deserve further investigation.

Acknowledgments. OA acknowledges supported by the Israeli Science Foundation grant 1022/21. AF and DJL acknowledge NERC grant NE/K014757/1 and NE/P013805/1. We thank Maya Shourky and Kaushal Gianchandani for helpful discussions.

Data availability statement. CMIP data was downloaded from the earth system grid (www.earthsystemgrid.org). ERA-Interim data was downloaded from the ECMWF public datasets repository (https://apps.ecmwf.int/datasets/). HadCM3L data is available at http://dx.doi.org/10.5194/cp-12-1181-2016-supplement.

References

Adam, O., 2018: Zonally varying ITCZs in a Matsuno–Gill-type model with an idealized Bjerknes feedback. *Journal of Advances in Modeling Earth Systems*, **10 (6)**, 1304–1318, https://doi.org/10.1029/2017MS001183.

Adam, O., 2021: Dynamic and energetic constraints on the modality and position of the intertropical convergence zone in an aquaplanet. *Journal of Climate*, **34 (2)**, 527–543.

Adam, O., T. Bischoff, and T. Schneider, 2016a: Seasonal and interannual variations of the energy flux equator and ITCZ. Part I: Zonally averaged ITCZ position. *J. Climate*, **29**, 3219–3230, https://doi.org/10.1175/JCLI-D-15-0512.1.

Adam, O., T. Bischoff, and T. Schneider, 2016b: Seasonal and interannual variations of the energy flux equator and ITCZ. Part II: Zonally varying shifts of the ITCZ. *J. Climate*, **29**, 7281–7293, https://doi.org/10.1175/JCLI-D-15-0710.1.

Adam, O., T. Schneider, and F. Brient, 2018a: Regional and seasonal variations of the double-ITCZ bias in CMIP5 models. *Climate Dynamics*, **51**, 101–117, https://doi.org/10.1007/s00382-017-3909-1.

Adam, O., T. Schneider, F. Brient, and T. Bischoff, 2016c: Relation of the double-ITCZ bias to the atmospheric energy budget in climate models. *Geophys. Res. Lett.*, **43**, 7670–7677.

Adam, O., and Coauthors, 2018b: The TropD software package (v1): standardized methods for calculating tropical-width diagnostics. *Geosci. Model Dev.*, **11**, 4339–4357, https://doi.org/10.5194/gmd-11-4339-2018.

Adler, R. F., and Coauthors, 2003: The Version-2 Global Precipitation Climatology Project (GPCP) monthly precipitation analysis (1979-present). *J. Hydrometeor.*, **4**, 1147–1167.

Atwood, A. R., A. Donohoe, D. S. Battisti, X. Liu, and F. S. Pausata, 2020: Robust longitudinally variable responses of the itcz to a myriad of climate forcings. *Geophysical Research Letters*, **47 (17)**, e2020GL088 833.

Bellucci, A., S. Gualdi, and A. Navarra, 2010: The double-itcz syndrome in coupled general circulation models: The role of large-scale vertical circulation regimes. *J. Climate*, **23 (5)**, 1127–1145, https://doi.org/10.1175/2009jcli3002.1.

Berry, G., and M. J. Reeder, 2014: Objective identification of the Intertropical Convergence Zone: Climatology and trends from the ERA-Interim. *J. Climate*, **27**, 1894–1909.

Bischoff, T., and T. Schneider, 2016: The equatorial energy balance, ITCZ position, and double ITCZ bifurcations. *J. Climate*, **29**, 2997–3013, https://doi.org/10.1175/JCLI-D-15-0328.1.

Bjerknes, J., 1969: Atmospheric teleconnections from the equatorial Pacific. *Mon. Wea. Rev.*, **97**, 163–172.

Blackburn, M., and Coauthors, 2013: The aqua-planet experiment (ape): Control sst simulation. *Journal of the Meteorological Society of Japan. Ser. II*, **91A**, 17–56, https://doi.org/10.2151/jmsj.2013-A02.

Bony, S., and Coauthors, 2015: Clouds, circulation and climate sensitivity. *Nature Geosci.*, **8**, 261–268.

Byrne, M. P., A. G. Pendergrass, A. D. Rapp, and K. R. Wodzicki, 2018: Response of the intertropical convergence zone to climate change: Location, width, and strength. *Current Climate Change Reports*, **4 (4)**, 355–370, https://doi.org/10.1007/s40641-018-0110-5.

Dee, D., and Coauthors, 2011: The ERA-Interim reanalysis: configuration and performance of the data assimilation system. *Quart. J. Roy. Meteor. Soc*, **137**, 553–597.

Deser, C., and J. M. Wallace, 1990: Large-scale atmospheric circulation features of warm and cold episodes in the tropical pacific. *Journal of Climate*, **3 (11)**, 1254–1281.

Diaz, H. F., and R. S. Bradley, 2004: The hadley circulation: present, past, and future. *The Hadley circulation: present, past and future*, Springer, 1–5.

Dima, I. M., and J. M. Wallace, 2003: On the seasonality of the Hadley cell. *J. Atmos. Sci.*, **60**, 1522–1527.

Donohoe, A., A. R. Atwood, and D. S. Battisti, 2021: Optimal geometric characterization of forced zonal mean tropical precipitation changes.

Donohoe, A., A. R. Atwood, and M. P. Byrne, 2019: Controls on the width of tropical precipitation and its contraction under global warming. *Geophysical Research Letters*, **46 (16)**, 9958–9967.

Donohoe, A., J. Marshall, D. Ferreira, and D. McGee, 2013: The relationship between ITCZ location and cross-equatorial atmospheric heat transport: From the seasonal cycle to the last glacial maximum. *J. Climate*, **26**, 3597–3618.

Eyring, V., S. Bony, G. A. Meehl, C. A. Senior, B. Stevens, R. J. Stouffer, and K. E. Taylor, 2016: Overview of the coupled model intercomparison project phase 6 (cmip6) experimental design and organization. *Geoscientific Model Development*, **9 (5)**, 1937–1958.

Frierson, D. M. W., and Y.-T. Hwang, 2012: Extratropical influence on ITCZ shifts in slab ocean simulations of global warming. *J. Climate*, **25**, 720–733.

Galanti, E., D. Raiter, Y. Kaspi, and E. Tziperman, 2022: Spatial patterns of the tropical meridional circulation: drivers and teleconnections. *Journal of Geophysical Research: Atmospheres*, e2021JD035531.

Goddéris, Y., Y. Donnadieu, G. Le Hir, V. Lefebvre, and E. Nardin, 2014: The role of palaeogeography in the phanerozoic history of atmospheric co2 and climate. *Earth-Science Reviews*, **128**, 122–138.

Gough, D., 1981: Solar interior structure and luminosity variations. *Physics of solar variations*, Springer, 21–34.

Gu, G., R. Adler, and A. Sobel, 2005: The eastern Pacific ITCZ during the boreal spring. *J. Atmos. Sci.*, **62**, 1157–1174.

Hannisdal, B., and S. E. Peters, 2011: Phanerozoic earth system evolution and marine biodiversity. *science*, **334 (6059)**, 1121–1124.

Harrison, S., P. Bartlein, K. Izumi, G. Li, J. Annan, J. Hargreaves, P. Braconnot, and M. Kageyama, 2015: Evaluation of cmip5 palaeo-simulations to improve climate projections. *Nat. Clim. Chang.*, **5**, 735–743, https://doi.org/10.1038/nclimate2649.

Jones, L. A., P. D. Mannion, A. Farnsworth, P. J. Valdes, S.-J. Kelland, and P. A. Allison, 2019: Coupling of palaeontological and neontological reef coral data improves forecasts of biodiversity responses under global climatic change. *Royal Society open science*, **6 (4)**, 182 111.

Kang, S. M., 2020: Extratropical influence on the tropical rainfall distribution. *Current Climate Change Reports*, 1–13.

Kim, H., S. M. Kang, K. Takahashi, A. Donohoe, and A. G. Pendergrass, 2021: Mechanisms of tropical precipitation biases in climate models. *Climate Dynamics*, **56 (1)**, 17–27.

Li, G., and S.-P. Xie, 2012: Origins of tropical-wide SST biases in CMIP multi-model ensembles. *Geophys. Res. Lett.*, **39**, L22 703.

Li, G., and S.-P. Xie, 2014: Tropical biases in CMIP5 multi-model ensemble: The excessive equatorial Pacific cold tongue and double ITCZ problems. *J. Climate*, **27**, 1765–1780.

Lin, J.-L., 2007: The double-ITCZ problem in IPCC AR4 coupled GCMs: Ocean–atmosphere feedback analysis. *J. Climate*, **20**, 4497–4525.

Lindzen, R. S., and A. Y. Hou, 1988: Hadley circulations for zonally averaged heating centered off the equator. *J. Atmos. Sci.*, **45**, 2416–2427.

Lindzen, R. S., and S. Nigam, 1987: On the role of sea surface temperature gradients in forcing low-level winds and convergence in the Tropics. *J. Atmos. Sci.*, **44**, 2418–2436.

Lunt, D. J., and Coauthors, 2016: Palaeogeographic controls on climate and proxy interpretation. *Climate of the Past*, **12 (5)**, 1181–1198.

Mechoso, C. R., and Coauthors, 1995: The seasonal cycle over the tropical pacific in coupled ocean-atmosphere general circulation models. *Mon. Wea. Rev.*, **123**, 2825–2838.

Medeiros, B., B. Stevens, and S. Bony, 2015: Using aquaplanets to understand the robust responses of comprehensive climate models to forcing. *Climate Dynamics*, **44 (7–8)**, 1957–1977, https://doi.org/10.1007/s00382-014-2138-0.

Möbis, B., and B. Stevens, 2012: Factors controlling the position of the intertropical convergence zone on an aquaplanet. *J. Adv. Model. Earth Syst.*, **4**, M00A04, https://doi.org/10.1029/2012MS000199.

Neelin, J. D., and I. M. Held, 1987: Modeling tropical convergence based on the moist static energy budget. *Mon. Wea. Rev.*, **115**, 3–12.

O'Brien, C. L., and Coauthors, 2017: Cretaceous sea-surface temperature evolution: Constraints from tex86 and planktonic foraminiferal oxygen isotopes. *Earth-Science Reviews*, **172**, 224–247.

Philander, S., D. Gu, D. Halpern, G. Lambert, N. Lau, T. Li, and R. Pacanowski, 1996: Why the ITCZ is mostly north of the equator. *J. Climate*, **9**, 2958–2972.

Popp, M., and N. Lutsko, 2017: Quantifying the zonal-mean structure of tropical precipitation. *Geophysical Research Letters*, **44 (18)**, 9470–9478.

Popp, M., and L. G. Silvers, 2017: Double and single ITCZs with and without clouds. *Journal of Climate*, **30 (22)**, 9147–9166.

Raiter, D., E. Galanti, and Y. Kaspi, 2020: The tropical atmospheric conveyor belt: A coupled eulerian-lagrangian analysis of the large-scale tropical circulation. *Geophysical Research Letters*, **47 (10)**, e2019GL086 437.

Rees, P. M., A. M. Ziegler, M. T. Gibbs, J. E. Kutzbach, P. J. Behling, and D. B. Rowley, 2002: Permian phytogeographic patterns and climate data/model comparisons. *The Journal of Geology*, **110 (1)**, 1–31.

Roberts, W., P. Valdes, and J. Singarayer, 2017: Can energy fluxes be used to interpret glacial/interglacial precipitation changes in the tropics? *Geophysical Research Letters*, **44 (12)**, 6373–6382.

Samuels, M., O. Adam, and H. Gildor, 2021: A shallow thermocline bias in the southern tropical pacific in cmip5/6 models linked to double-itcz bias. *Geophysical Research Letters*, **48 (15)**, e2021GL093 818.

Schneider, T., T. Bischoff, and G. H. Haug, 2014: Migrations and dynamics of the intertropical convergence zone. *Nature*, **513**, 45–53, https://doi.org/10.1038/nature13636.

Staten, P. W., J. Lu, K. M. Grise, S. M. Davis, and T. Birner, 2018: Re-examining tropical expansion. *Nature Climate Change*, **8 (9)**, 768–775.

Talib, J., S. Woolnough, N. Klingaman, and C. Holloway, 2018: The role of the cloud radiative effect in the sensitivity of the intertropical convergence zone to convective mixing. *J. Climate*, **31**, 6821–6838, https://doi.org/10.1175/JCLI-D-17-0794.1.

Taylor, E. L., T. N. Taylor, and N. R. Cúneo, 1992: The present is not the key to the past: a polar forest from the permian of antarctica. *Science*, **257 (5077)**, 1675–1677.

Taylor, K. E., R. J. Stouffer, and G. A. Meehl, 2012: An overview of cmip5 and the experiment design. *Bulletin of the American meteorological Society*, **93 (4)**, 485–498.

Tian, B., and X. Dong, 2020: The double-itcz bias in cmip3, cmip5, and cmip6 models based on annual mean precipitation. *Geophysical Research Letters*, **47 (8)**, e2020GL087 232.

Trenberth, K. E., and J. T. Fasullo, 2012: Tracking Earth's energy: From El Niño to global warming. *Surv. Geophys.*, **33**, 413–426.

Valdes, P. J., and Coauthors, 2017: The bridge hadcm3 family of climate models: Hadcm3@ bristol v1. 0. *Geoscientific Model Development*, **10 (10)**, 3715–3743.

van der Wiel, K., A. J. Matthews, and D. P. Stevens, 2016: Why the South Pacific Convergence Zone is diagonal. *Clim. Dyn.*, **46 (5)**, 1683–1698, https://doi.org/10.1007/s00382-015-2668-0.

Vincent, D. G., 1994: The south pacific convergence zone (spcz): A review. *Monthly weather review*, **122 (9)**, 1949–1970.

Voigt, A., S. Bony, J.-L. Dufresne, and B. Stevens, 2014: The radiative impact of clouds on the shift of the intertropical convergence zone. *Geophys. Res. Lett.*

Webster, P. J., 2020: *Dynamics of the Tropical Atmosphere and Oceans*. John Wiley & Sons.

Wilks, D. S., 2011: *Statistical methods in the atmospheric sciences*, Vol. 100. Academic press.

Xie, P., and P. Arkin, 1996: Analyses of global monthly precipitation using gauge observations, satellite estimates, and numerical model predictions. *J. Climate*, **9**, 840–858.

Yan, H., W. Wei, W. Soon, A. Zhisteng, W. Zhou, Z. Liu, Y. Wang, and R. Carterm, 2015: Dynamics of the intertropical convergence zone over the western Pacific during the Little Ice Age. *Nature Geoscience*, **8**, 315–320.

Zhang, C., 2001: Double ITCZs. *Journal of Geophysical Research: Atmospheres*, **106 (D11)**, 11 785–11 792.

Zhang, H., R. Seager, and S.-P. Xie, 2022: How does sea surface temperature drive the intertropical convergence zone in the southern indian ocean? *Journal of Climate*, 1–40.

Zhao, B., and A. Fedorov, 2020: The seesaw response of the intertropical and south pacific convergence zones to hemispherically asymmetric thermal forcing. *Climate Dynamics*, **54 (3)**, 1639–1653.

Zheng, Y., J.-L. Lin, and T. Shinoda, 2012: The equatorial Pacific cold tongue simulated by IPCC AR4 coupled GCMs: Upper ocean heat budget and feedback analysis. *J. Geophys. Res.*, **117**, C05 024, https://doi.org/10.1029/2011JC007746.